Acid-Induced Equilibrium Folding Intermediate of Human Platelet Profilin[†]

Glendon D. McLachlan, Sean M. Cahill, Mark E. Girvin, and Steven C. Almo*

Department of Biochemistry, Albert Einstein College of Medicine, 1300 Morris Park Avenue, Bronx, New York 10461

Received February 3, 2006; Revised Manuscript Received May 14, 2006

ABSTRACT: The acid-induced unfolding of human platelet profilin (HPP) can be minimally modeled as a three-state process. Equilibrium unfolding studies have been performed on human platelet profilin1 (HPP) and monitored by far-UV circular dichroism, tryptophan fluorescence, ANS binding, and NMR spectroscopy. Far-UV CD measurements obtained by acid titration demonstrate that HPP unfolds via a three-state mechanism (N $\rightarrow$ I $\rightarrow$ U), with a highly populated intermediate between pH 4 and 5. Approximately 80% of native helical secondary structural content remains at pH 4, as indicated by monitoring the CD signal at 222 nm. The stability (ΔG_{H2O}) of the native conformation at pH 7.0 (obtained by monitoring the change in tryptophan signal as a function of urea concentration) is 5.56 ± 0.51 kcal mol^{-1}; however, the ΔG_{H2O} for the intermediate species at pH 4 is 2.01 ± 0.47 kcal mol^{-1}. The calculated *m*-values for the pH 7.0 and pH 4.0 species were 1.64 ± 0.15 and 1.34 ± 0.17 kcal mol^{-1} M^{-1}, respectively, which is an indication that the native and intermediate species are similarly compact. Additionally, translational diffusion measurements obtained by NMR spectroscopy and ANS binding studies are consistent with a globular and compact conformation at both pH 7.0 and 4.0. The pK_a values for the two histidine (His) residues located on helix 4 of HPP were determined to be 5.6 and 5.7 pH units. These pK_a values coincide with the midpoint of the far-UV CD acid titration curve and suggest that the protonation of one or both His residues may play a role in the formation of the unfolding intermediate. Stable intermediate species populate the 2D ^{1}H-^{15}N HSQC NMR spectra between pH 4 and 5. A number of backbone and side-chain resonances show significant perturbations relative to the native spectrum; however, considerable nativelike tertiary contacts remain. Interestingly, the residues on HPP that are significantly altered at low pH coincide with segments of the G-actin binding surface and poly-L-proline binding interface. The earlier reports that a decrease in pH below 6.0 induces structural alterations in profilin, favoring dissociation of the profilin−actin complex, corresponds with the structural alterations observed in the partially unfolded species. Our findings suggest that a novel mechanism for pH induced disruption of the profilin−G-actin complex involve a nativelike unfolding intermediate of profilin.

Dynamic remodeling of the actin cytoskeleton is essential for cell locomotion, cytokinesis, complex morphogenetic and developmental programs in multicellular organisms, and pathological states such as neoplastic transformation and tumor metastasis. These processes rely on the coordination of signaling pathways that control the activity and subcellular localization of the proteins that regulate the assembly, disassembly, and function of distinct filamentous actin (F-actin) structures. Of particular importance are the profilins (∼12−15 kDa), an evolutionarily conserved and essential family of actin monomer (G-actin) binding proteins. All profilins share the same basic architecture, which is built around an antiparallel β-sheet, sandwiched between two α-helical segments on each side (Figure 1) (*1−3*). In mammals, two isoforms (profilin1 and profilin2) have been identified that exhibit distinct expression patterns, with profilin2 preferentially expressed in brain tissue and profilin1 (also referred to as platelet profilin) being present in all tissue
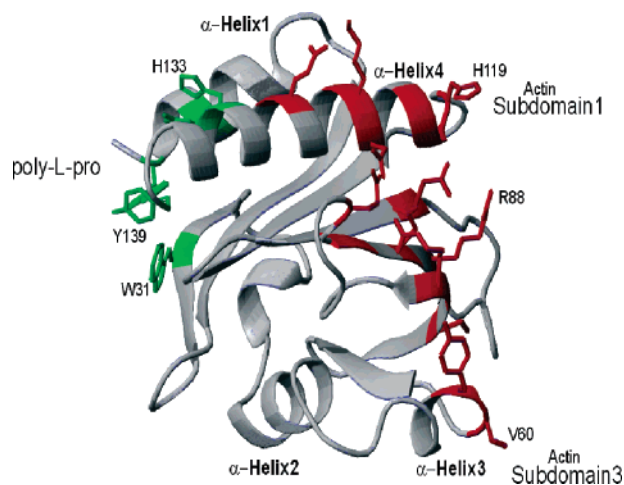

FIGURE 1: Ribbon diagram representation of the X-ray crystal structure of HPP. The 3D fold of the polypeptide chain consists of a compact α/β sandwich with seven antiparallel β-strands and four α-helices. The backbone atoms are colored gray, and the residues involved in actin and poly-L-proline binding are shown in red and green, respectively. Molmol was used to generate this ribbon diagram.

* To whom correspondence should be addressed. Tel: (718) 430-2746. Fax: (718) 430-8565. E-mail: almo@aecom.yu.edu.

types (*4*). The profilin isoforms also exhibit different physical characteristics and display different biochemical properties

toward known in vivo ligands, suggesting specialized functions and regulatory mechanisms (*5*). Profilin has been proposed to regulate actin filament assembly in vivo through several mechanisms including monomer sequestration, the ability to increase the available pool of monomeric actin for barbed end addition, and the enhancement of adenine nucleotide exchange on G-actin (*6*−*10*). As F-actin depolymerization results in the release of ADP-actin monomers, this latter activity may be particularly important for the regeneration of polymerization competent ATP-actin monomers.

Profilin also binds to polyphosphoinositides, such as phosphatidylinositol-4,5-bisphoshate (PIP_2). This interaction is of considerable importance because PIP_2 competes with actin for binding to profilin, resulting in a disruption of the profilin−actin complex. Furthermore, biochemical evidence shows that the binding of profilin to PIP_2 inhibits the PLCγ-mediated hydrolysis of PIP_2 to the second messengers diacylglycerol and IP_3 (*11*, *12*). Thus, profilin may directly link the organization of the actin cytoskeleton with phosphoinositide metabolism. Additionally, profilin binds to highly proline-rich sequences present in a number of signaling and scaffolding proteins found at the leading edge of motile cells, including members of the VASP/Mena and formin families, and these interactions are thought to be involved in correctly localizing profilin to sites of active F-actin polymerization (*13*−*18*).

Recent evidence supports a role for the interaction with PIP_2 in localizing profilin to the plasma membrane (*19*−*21*), and interactions with proline-rich targeting sequences may provide an additional mechanism for directing profilin to the vicinity of the plasma membrane. A complete understanding of the structural and functional consequences of these profilin−lipid interactions requires a detailed consideration of the solution properties immediately proximal to the phospholipids of the inner leaflet. Experimental and theoretical approaches suggest that the local pH immediately proximal to the inner leaflet of the plasma membrane may be as much as 0.5−2 pH units lower than the bulk cytoplasmic pH (*22*, *23*). The proposed low pH is purported to be the consequence of the high local concentration of acidic phospholipids in the inner leaflet, which directs local recruitment of protons and results in a locally reduced pH that persists for ∼15 Å from the membrane surface (*23*, *24*). Importantly, the experimental and computational efforts that support this reduced pH are based solely on the consideration of monoanionic acidic phospholipids in the inner leaflet. Even greater effects might be expected from rafts of polyanionic polyphosphoinositides such as PIP_2, which are known to accumulate in regions of extensive actin dynamics (*25*, *26*).

Considerable evidence from studies involving artificial model membranes supports a physiological role for the phospholipid-associated pH gradient and electrical potential. The reduced pH immediately proximal to the plasma membrane affords the opportunity for cytoplasmic proteins to achieve non-native conformations, which Ptitsyn has suggested may play a role in a wide range of biological processes, including membrane insertion and translocation, chaperone-assisted transport and folding, and protein degradation (*27*). Specific examples include the native to molten globule transition associated with the insertion of the bacterial toxins (e.g., colicin A (*22*) and diptheria toxin (*28*)) into membranes, protein unfolding events required for the transport of precursor proteins across the mitochondrial inner membrane (*29*), and the structural integrity of proteins involved in electron transport (i.e., cytochrome *c*) (*24*).

To gain an understanding of the potential functional consequence of the putative reduced membrane-proximal pH on the regulation of the actin cytoskeleton, we have examined the equilibrium structural behavior of HPP[1] as a function of pH, using circular dichroism (CD), fluorescence, and NMR. These studies demonstrate a three-state unfolding transition with an initial transition beginning at pH ∼6.5 that results in a fully populated equilibrium intermediate at pH 4−5, with a second transition below pH 4 leading to the fully denatured state. The residues most perturbed as the pH is lowered cluster around the actin binding surface, suggesting that the membrane proximal environment could regulate the profilin−actin interaction.

MATERIALS AND METHODS

Chemicals and Reagents. Ultrapure urea was purchased from Sigma. ^{15}N-ammonium chloride, D_2O, DCl, and NaOD were purchased from Cambridge Isotopes (Cambridge, Massachusetts). Double distilled deionized water was used in all experiments. All additional chemicals were of reagent grade.

Human Platelet Profilin (HPP) Purification. Recombinant ^{15}N-labeled and unlabeled HPP were prepared as previously described (*30*). Briefly, *E. coli* BL21 (DE3) cells were transformed with the pMW172-based expression vector and grown in either Luria broth (LB) or M9 minimal media containing ^{15}N-ammonium chloride as the sole nitrogen source. HPP was purified by poly-L-proline affinity chromatography and homogeneity (>95%) was confirmed by SDS poly-acrylamide gel electrophoresis. The expression of HPP in LB and minimal media yielded approximately 40 and 25 mg/L, respectively.

Sample Preparations. For NMR spectroscopy, the sample buffer was exchanged from 10 mM Tris-KCl to 10 mM citrate-phosphate, and the pH was adjusted by dialysis at 4 °C. The protein was concentrated using a 3000 Dalton cutoff Centricon filter, and the final protein concentrations used in the NMR experiments were 0.5−1.0 mM in a sample volume of 600 μL.

Samples for the histidine titration studies were prepared by adding 600 μL of a 0.2 mM stock of unlabeled HPP in 10 mM citrate-phosphate buffer to a 10 mM citrate-phosphate buffer in 100% D_2O, up to a final volume of 2 mL. The diluted sample was concentrated to 600 μL and the dilution/concentration cycle repeated three times to deuterate all exchangeable ^1H nuclei. The pD of the diluted samples was adjusted by adding NaOD or DCl and monitored with an Orion digital pH meter without corrections.

The samples for the pH titration of HPP monitored by CD were prepared by adding 100 μM purified HPP in 10 mM citrate-phosphate buffer at pH 7.2 (final concentrations of 10−20 μM) to Eppendorf tubes containing 10 mM citrate-

---

phosphate buffer (pre-filtered with a 0.25 μm filter) and 1 mM DTT with the pH preset between 2.0 and 8.0 units. The fluorescence studies were conducted using 5 μM protein. The samples were prepared at each pH in triplicate and allowed to equilibrate overnight at room temperature. Importantly, the pH was measured before and after data collection for consistency. Purified HPP in 10 mM Tris buffer was used for experiments conducted at pH 8.0.

The urea denaturation studies at pH 4.0 and 7.0 were performed with HPP at final concentrations of 10−20 μM and buffered in 10 mM citrate-phosphate and 1 mM DTT. Protein solutions containing 0−8 M urea were allowed to equilibrate overnight at room temperature and CD/fluorescence spectra were collected as described below.

2D ^{1}H-^{15}N HSQC NMR Spectroscopy. All NMR experiments were performed at 20 °C on a Bruker DRX 600 MHz spectrometer equipped with a 5 mm inverse triple resonance three axis gradient probe. 2D ^{1}H-^{15}N gradient selected sensitivity-enhanced HSQC spectra were collected with 4K complex points in F2 (^{1}H) and 256 complex points in F1 (^{15}N) dimensions, with 32 scans per t1 point and a recycle delay of 1.3 s (*31*). All experiments used a proton sweep width of 14 ppm and a ^{15}N sweep width of 40 ppm with the ^{1}H and ^{15}N carriers set to 4.7 and 120 ppm, respectively. Spectra were processed with a cosine bell window function and zero filled to yield data sets with 4K and 512 points in F2 (^{1}H dimension) and F1 (^{15}N dimension), respectively. Proton chemical shifts were referenced to internal 3-(trimethylsilyl) propionate (TSP).

Pulsed Field Gradient NMR Self-Diffusion Experiment. Pulse field gradient (PFG) self-diffusion measurements (*32*) were recorded at pH 7.0, 4.0, and 2.0 on a DRX-600 MHz spectrometer. Diffusion measurements were recorded on 0.7 mM ^{15}N-labeled HPP in 10 mM citrate-phosphate buffer (90% H_2O/10% D_2O) at 20 °C. A total of 16 spectra were acquired, with increasing PFG strength. The gradient delay used was 4.0 ms. The self-diffusion coefficient (D_s) is obtained from a fit of the signal decay to the relationship

$$A\,(2\tau) = A(0)\,\exp[-(\gamma\delta\Gamma)^2\,(\Delta-\delta/3)D_s] \qquad (1)$$

where $\gamma = {}^1$H gyromagnetic ratio, δ = PFG duration (s), Γ = gradient strength (G/cm), Δ = time between PFG pulse (s), and A (2τ) = the echo amplitude. The gradient strength was calibrated by measuring decay curves on a lysozyme sample in D_2O and using a literature value of 1.08 cm^2 s^{-1} for the self-diffusion coefficient (*33*).

Histidine Titration. 1D ^{1}H NMR experiments for histidine titration studies were performed on a Bruker DRX-300 MHz spectrometer at 20 °C. Spectra were collected using WATERGATE water suppression with a total of 64 scans and a sweepwidth of 14 ppm, sampled with 1024 complex points and a recycle delay of 1.3 s. (*34*). Spectra were processed with a cosine bell window function, zero filled to 2048 points and were baseline corrected. The pK_a values were determined from fits of the Henderson−Hasselbach equation to a plot of the chemical shift change as a function of pH (assuming a single titrating group):

$$\delta(\text{pH}) =$$
$$\delta(\text{neutral}) + \Delta\delta[10^{(\text{p}K_a-\text{pH})}]/[1 + 10^{(\text{p}K_a-\text{pH})}] \quad (2)$$

where δ = chemical shift and $\Delta\delta$ = chemical shift difference between charged and neutral species. KaleidaGraph 3.0 was used for all curve-fitting procedures.

Circular Dichroism. All CD spectra were collected on a Jasco 720 spectropolarimeter at room temperature using either 1 mm or 5 mm path length quartz cuvettes. The concentrations used were 10−20 μM (0.33−0.67 mg/mL). Each spectrum was baseline corrected by subtracting the buffer spectrum, and the data were analyzed without spectral smoothing. The molar ellipticity was calculated according to $[\theta] = \theta_\lambda/10dc_r$, where θ_λ is the ellipticity in millidegrees, d is the cuvette path length in cm, and c_r is the mean residue molar concentration in mol/mL. Three independent measurements, taken at 0.5 nm intervals, were recorded and averaged for each spectral point in all experiments.

The fraction unfolded ($\mathbf{f}_u$) was calculated based on the ratio

$$\mathbf{f}_{u\,=}(Y - Y_n)/(Y_d - Y_n)$$

where Y = ellipticity observed at a specific [urea], Y_n = ellipticity of the folded protein, and Y_d = ellipticity at 8 M urea.

The unfolding free energy change at zero molar urea ($\Delta G_{(H2O)}$) was obtained from nonlinear least-squares fits to the data points with baseline corrections based on the methods of Santoro and Bolen, according to the equation below (*35*). The analysis assumes a two-state model for unfolding and a reversible process.

$$Y = \{(y_n + m_n[\text{urea}]) + (y_u + m_u[\text{urea}])$$
$$\exp[-(\Delta G_{(H2O)}/RT + m_G[\text{urea}]/RT)]\}/$$
$$\{1 + \exp[-(\Delta G_{(H2O)}/RT + m_G[\text{urea}]/RT)]\} \quad (3)$$

where $\Delta G_{(H2O)}$ represents the free energy change in the absence of urea, m_G is the ΔG dependence on urea concentration, y_n and y_u are the baseline intercepts for the native and unfolded forms, respectively, extrapolated to zero urea, and m_n and m_u represent the slopes of the fitted baselines. The gas constant R has units of kcal mol^{-1} K^{-1}, and the temperature T is in Kelvin.

Intrinsic Tryptophan Fluorescence. Data were collected on 5 μM samples of HPP at room temperature using a Photon Technology International (PTI) spectrofluorometer, model QM-4/2005. The slit-widths were set at 2 nm, the excitation wavelength was set at 295 nm, and the emission spectrum was recorded from 305 to 400 nm in 0.5 nm increments. Spectra were corrected for background contributions by subtracting scans of samples containing only the buffer at each pH.

ANS Fluorescence Spectroscopy. Exposed hydrophobic surface area was probed by 8-anilinonaphthalene-1-sulfonate (ANS) binding. Experiments were conducted at room temperature with 5 μM HPP and 50 μM ANS in 10 mM citrate-phosphate and 1 mM DTT. The excitation wavelength was set at 385 nm, and the emission sweep-width was from 400 to 600 nm, with a 2 nm slit-width.

RESULTS

Acid-Induced Unfolding of HPP Monitored by CD at 222 nm. As judged by CD, the acid-induced unfolding of HPP is consistent with a minimal three-state process, i.e.,
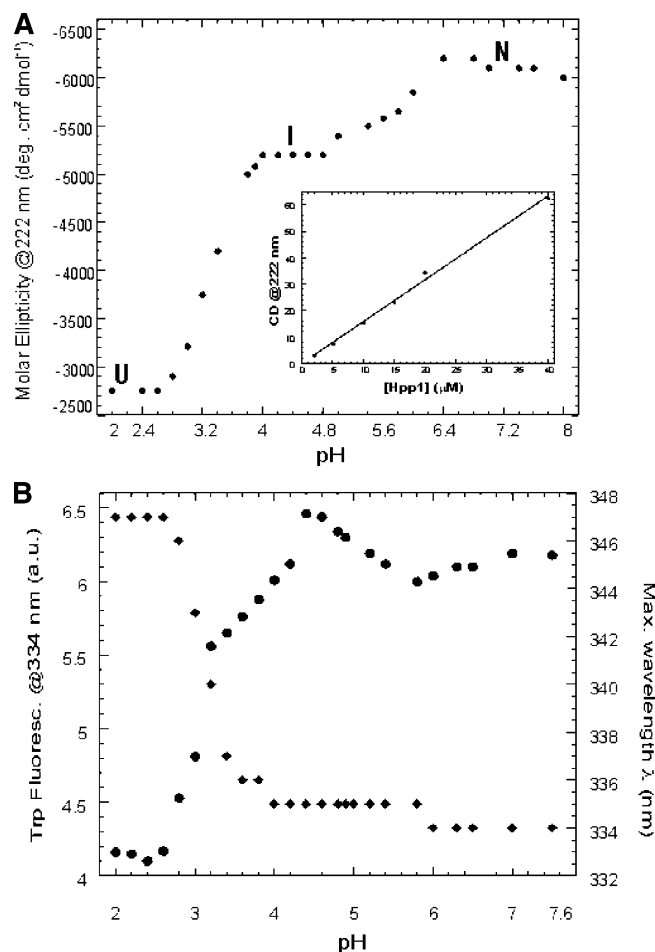
FIGURE 2: Acid titration of HPP monitored by far-UV circular dichroism spectroscopy and intrinsic tryptophan fluorescence. (A) Equilibrium unfolding of HPP (in 10 mM citrate-phosphate buffer and 1 mM DTT at room temperature) monitored by the change in molar ellipticity at 222 nm reveals that HPP unfolds in multiple stages. The CD trace results from a plot of the average molar ellipticity of three experiments (standard deviations less than 5%) and shows that HPP unfolds in two discreet steps (N → I → U) with a stable intermediate population between pH 4.0 and 5.0. The inset shows a linear plot of the CD signal as a function of protein concentration. (B) Tryptophan fluorescence at 334 nm (●) (left axis) and the wavelength at maximum fluorescence (◆) as a function of pH. The experimental conditions were identical to those used in the CD measurements except that 5 μM of HPP was used for fluorescence measurements.

N → I → U. The first transition begins at ~pH 6.5 with an equilibrium intermediate being fully populated between pH 5.0 to 4.0 (Figure 2). The transition midpoint from the native state to intermediate state occurs at approximately pH 5.8, which suggests that ionizeable groups with pK_a values in this range are involved in the partial unfolding of HPP (N → I). The second transition midpoint occurs close to pH 3.4, suggesting that protonation of the side-chain carboxylate groups of Asp and Glu may be involved in the transformation to the unfolded state (I → U). The molar ellipticity at 222 nm (i.e., α-helix content) for the equilibrium unfolding intermediate (pH 4.4) is approximately 84% of that of the native state (pH 7.0). This observation indicates that the average α-helical content of the unfolding intermediate is comparable to that of the native state.

To rule out the possibility that aggregation contributed to the observed phenomena, a concentration dependence study

of the pH 4.4 species was performed at room temperature and monitored by the CD at 222 nm (Figure 2, inset). The linear relationship between CD and concentration indicates that aggregation is not involved in the formation of the unfolding intermediate at the protein concentrations used.

Acid Titration of HPP Monitored by Tryptophan Fluorescence. The intrinsic tryptophan fluorescence intensity and wavelength maximum are useful probes for monitoring protein structural fluctuations and conformation dynamics. The two tryptophan residues on HPP, tryptophan 3, and tryptophan 31, map to a solvent exposed hydrophobic surface, with tryptophan 31 being partially buried at the edge of β-strand 2. Consistent with this environment, the average maximum tryptophan-fluorescence signal was measured at a wavelength of 334 nm for the native species. The fluorescence intensity profile verses pH is complex (Figure 2B). The tryptophan fluorescence maximum occurs between pH 4.4 and 4.6 and is accompanied by a minor red shift in λ_{max}, suggesting that the observed fluorescence change is not due to the increased exposure of the indole group to solvent but is due to structural modifications within a less rigid hydrophobic surface. The modest shift in λ_{max} is further evidence that a similar degree of solvent exposure of the tryptophan in the native species is maintained in the exposed hydrophobic surface of the intermediate ensemble. A transition occurs from the intermediate ensemble to the unfolded state below pH 3.0, as indicated by fluorescence quenching and red shifted λ_{max} to 347 nm.

ANS Binding as a Function of pH. To detect changes in the solvent accessibility of the hydrophobic core of HPP and the resulting loss of tertiary structure during the unfolding transition, the fluorescence of the hydrophobic dye ANS was monitored with decreasing pH. ANS is a fluorescent dye that has been used extensively to probe exposed, ordered hydrophobic surfaces on partially folded polypeptides (*36*). In aqueous solutions, ANS fluorescence is minimal; however, the fluorescence is enhanced many fold with a concomitant blue shift in wavelength (below 500 nm) when bound within a hydrophobic cavity. Consistent with this behavior, a fully folded or unfolded protein exhibits minimal interaction with ANS; in contrast, interactions are maximal with partially folded species (*36*). Figure 3A and B show plots of the ratio of ANS fluorescence (F/F_0) in the presence and absence of HPP and the associated shift in emission wavelength from pH 7.5 to 2.2. Figure 3C shows the pH titration of ANS from pH 2 to 8, which does not exhibit pH dependence. Relative to the ANS fluorescence alone, the fluorescence change from pH 7.5 to 5.5 in the presence of HPP is negligible. However, the ANS fluorescence is enhanced at pH 5.0 by 3-fold, and a 7-fold increase in fluorescence is observed at pH 4.0. More dramatically, a fluorescence enhancement of 35-fold is observed at pH 3.75, and the maximum fluorescence is observed at pH 3.0 with an increase of 39-fold relative to that of ANS alone. Over this range, the wavelength of the fluorescence maximum is also blue-shifted from 500 to 470 nm. The enhanced ANS fluorescence at pH 5.0 and below indicates an increase in hydrophobic surface area interaction, and the blue shifted wavelength is evidence that the tertiary fold of the intermediate species is disrupted relative to the native fold. Notably, the ANS fluorescence emission spectra of the intermediate species populated between pH 4 and 5 are more similar to the native
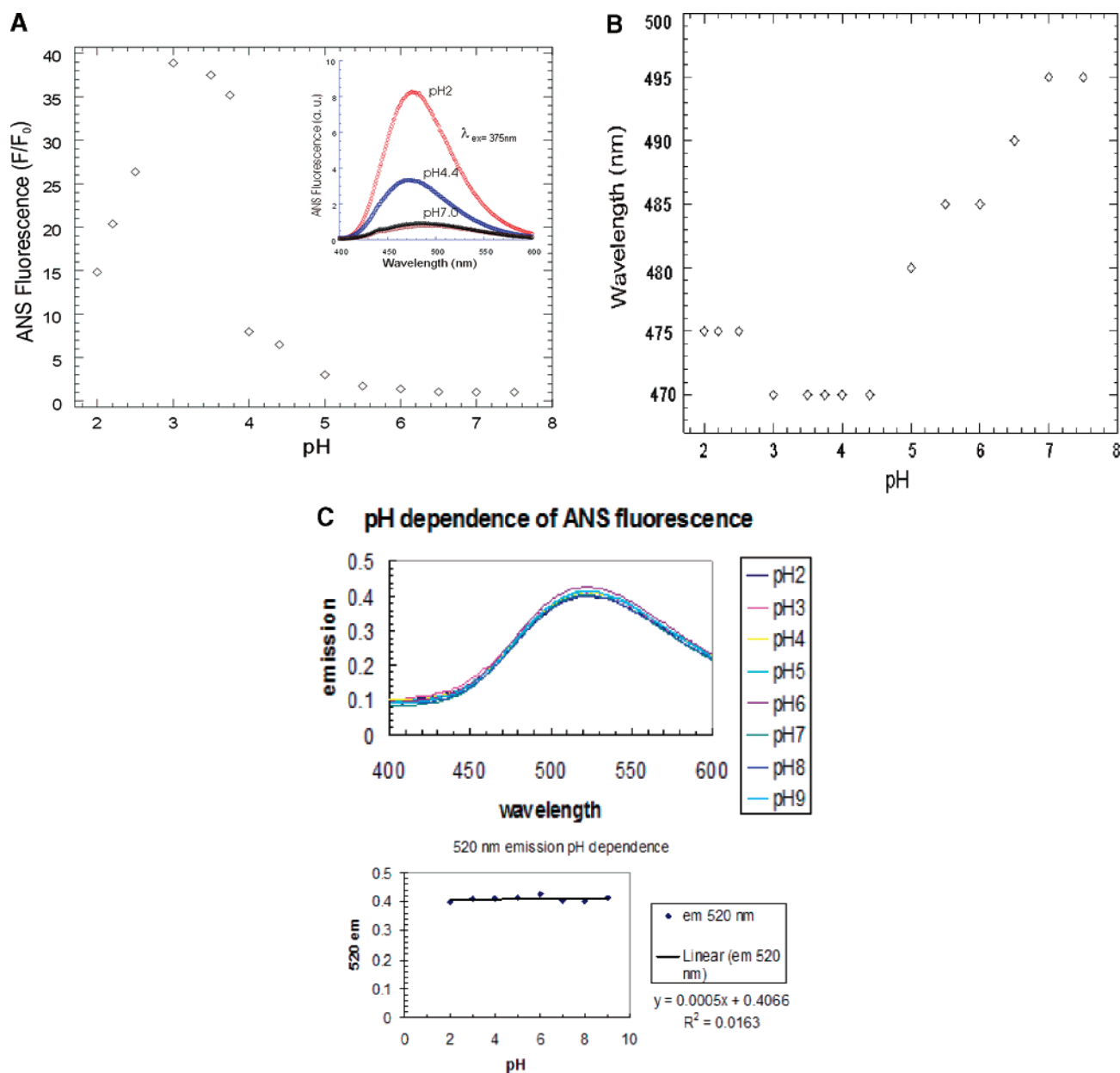
FIGURE 3: The relative change in ANS fluorescence emission maximum in the absence and presence of HPP. (A) Ratio of ANS fluorescence emission intensity in the presence and absence of HPP as a function of pH at 10:1 ANS to HPP (excitation: 375 nm). The inset shows the superposition of ANS fluorescence spectra of ANS in buffer (brown), ANS plus HPP at pH 7 (black), pH 4.4 (blue) and pH 2 (red). (B) Plots of the change in maximum wavelength (λ_{max}) as a function of pH. (C) Fluorescence of ANS alone from pH 2 to 9, along with a plot of the change in emission in this pH range.

species than the species at pH 3.0, indicating that the native structure and equilibrium intermediate share a similar proportion of exposed hydrophobic surface and compactness. The ANS fluorescence enhancement decreases as the pH is lowered below 3.0 and is red-shifted from 470 to 475 nm, which signals a decrease in available ordered, hydrophobic binding surface. The inset in Figure 3A shows the emission spectra of ANS only and ANS in the presence of HPP at pH 7.0, 4.4, and 2.2.

Chemical Denaturation of HPP Monitored by CD. To determine the stability of the pH 7.0 and 4.0 thermodynamic states, chemical denaturation using urea was monitored by CD at 222 nm. Figure 4A and B shows the behavior of the native state and the equilibrium intermediate, respectively, presented as the fraction unfolded as a function of urea concentration. The fitting assumes a two-state transition for

each process. The extrapolated values from best fits to the data points are shown in Table 1. The $\Delta G_{(H2O)}$ of HPP at pH 7.0 was determined to be 6.59 ± 1.1 kcal mol^{-1}, and the value obtained for the pH 4.0 species was 4.01 ± 0.62 kcal mol^{-1} with unfolding midpoints of 3.25 and 2.25 M urea, respectively. At equilibrium, both the native and intermediate species are fully populated relative to the unfolded species, with the intermediate species ~99% populated ($K_{eq} = \exp-(\Delta G/RT) = 0.0011$). Additionally, m-values of 2.08 ± 0.35 and 1.89 ± 0.24 kcal mol^{-1} M^{-1} urea were obtained for the native and intermediate states, respectively. The m-value is a measure of the dependence of ΔG on urea concentration and reports on the relative compactness of the polypeptide chain. These results indicate that the pH 4 conformation is compact and stable and represents a distinct non-native population.
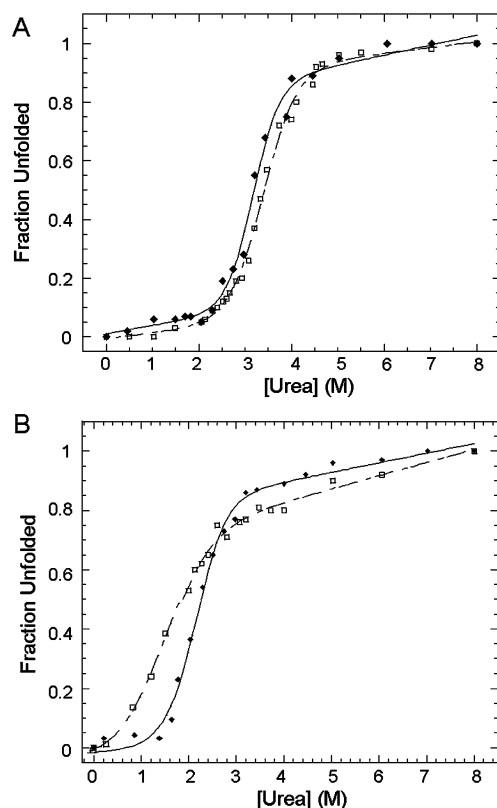
FIGURE 4: Urea unfolding of HPP monitored by tryptophan fluorescence and CD spectroscopy. (A) Plots of the change in intrinsic tryptophan fluorescence (□) and molar ellipticity (◆) with increasing urea concentration at pH 7.0 and 6.5 shows two-state behavior with midpoints at 3.4 M urea for the tryptophan signal and 3.25 M urea for the change in ellipticity. The ΔG_{H2O} values extrapolated from the nonlinear least-squares fit (assuming a two-state transition from N → U) of the tryptophan fluorescence and CD data points are 5.56 ± 0.51 and 6.59 ± 1.10 kcal mol^{-1}, respectively. (B) Equilibrium unfolding of HPP at pH 4.0 monitored by tryptophan fluorescence at 360 nm (□) and CD at 222 nm (◆). The data represents the fraction unfolded as a function of urea concentration. The ΔG_{H2O} values obtained from a nonlinear least-squares analysis of the titration curves for tryptophan fluorescence and CD are 2.01 ± 0.47 and 4.01 ± 0.62 kcal mol^{-1} with the unfolding midpoint occurring at 1.8 and 2.25 M urea, respectively. The concentrations of HPP used in the CD and fluorescence studies were 15 and 10 μM, respectively.

Chemical Denaturation of HPP Monitored by Intrinsic Tryptophan Fluorescence. The conformational stability of HPP was also determined by monitoring the intrinsic tryptophan fluorescence at 360 nm with increasing urea concentration. Figure 4A and B shows the relative fluorescence for native HPP (pH 7.0) and the intermediate species (pH 4.0). Values for $\Delta G_{(H2O)}$ were obtained from a nonlinear least-squares fit of the data points. The extrapolated $\Delta G_{(H2O)}$ at pH 7.0 was 5.56 ± 0.51 kcal mol^{-1}, with an *m*-value of 1.64 ± 0.15 kcal mol^{-1} M^{-1}, and the $\Delta G_{(H2O)}$ at pH 4.0 was 2.01 ± 0.47 kcal mol^{-1} with an *m*-value of 1.34 ± 0.17 kcal mol^{-1} M^{-1}. The unfolding midpoints occurred at 3.4 M urea and 1.8 M urea for the pH 7 and 4 species, respectively; however, the *m*-value differs by only 18%, indicating that the global fold and compaction of the intermediate state is near native. Moreover, a significantly populated equilibrium intermediate (∼88% relative to the unfolded state) exists at pH 4, relative to that in the unfolded state. Overall, the urea unfolding curves of HPP monitored

Table 1: Thermodynamic Data for Native and Intermediate HPP

probe	pH	ΔG_{H2O} (kcal mol^{-1})[a]	*m*-value (kcal mol^{-1} M^{-1})[b]	C_m (M)[c]
CD	6.5	6.59 ± 1.1	2.08 ± 0.35	3.25
	4.0	4.01 ± 0.62	1.89 ± 0.24	2.25
tryptophan	7.0	5.56 ± 0.51	1.64 ± 0.15	3.4
	4.0	2.01 ± 0.47	1.34 ± 0.17	1.80

[a] Free energy of unfolding extrapolated to 0 M urea. [b] Change in ΔG as a function of urea concentration. [c] Midpoint of unfolding titration curve.
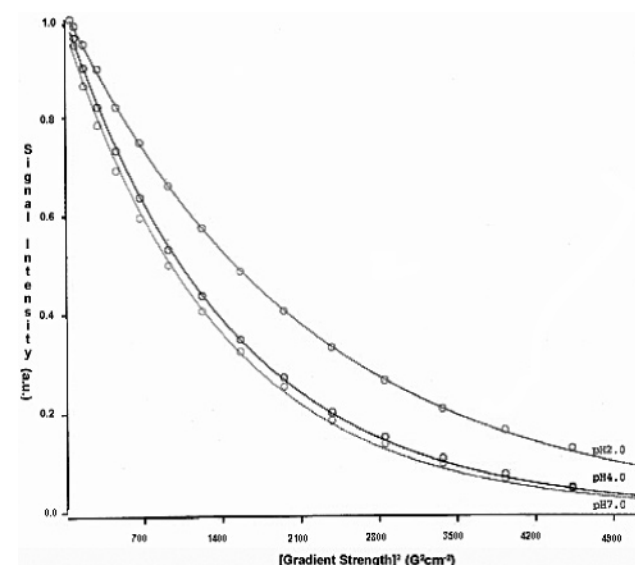
FIGURE 5: Pulsed field gradient translational diffusion measurements of HPP at pH 7, 4, and 2. The attenuation of the signal intensity as a function of gradients for 0.5 mM HPP in 10 mM citrate-phosphate buffer and 1 mM DTT at room temperature is shown. The decay curves for the native conformation at pH 7 and the unfolded species at pH 2 are colored gray, and the curve for the intermediate species at pH 4 is colored black.

by far-UV CD and tryptophan fluorescence for the native species (pH 7) are similar, suggesting a cooperative mechanism for unfolding. In contrast, the unfolding curves for the pH 4.0 species do not coincide, indicating that unfolding proceeds in a noncooperative manner with the loss of tertiary structure preceding the loss of secondary structure.

Pulsed Field Gradient Translational Diffusion Measurements. To determine whether NMR spectroscopic measurements of the equilibrium unfolding intermediate were feasible at high protein concentration (i.e. without aggregating), pulsed field gradient self-diffusion measurements were made with 0.71 mM HPP at pH 4.2 and 20 °C. Similar measurements were taken for the pH 7.0 and 2.0 species at concentrations of 0.71 and 0.66 mM, respectively, for direct comparison. The 1D-^{1}H spectra of HPP at pH 7 and 4.2 are well resolved with sharp lines in the amide and aliphatic regions. A typical plot of the signal attenuation as a function of gradient strength for a single nonoverlapping resonance is shown in Figure 5 for the pH 7, 4, and 2 species. Diffusion coefficients (D_s) of 1.04 × 10^{-6} cm^2/s ± 0.01 and 1.12 × 10^{-6} cm^2/s ± 0.01 were determined for the pH 4.0 and 7.0 species, respectively. Similar D_s values have been calculated for globular polypeptide chains with molecular weights of approximately 15−20 (assuming a spherical arrangement) (*32*). The measured D_s for the equilibrium intermediate is
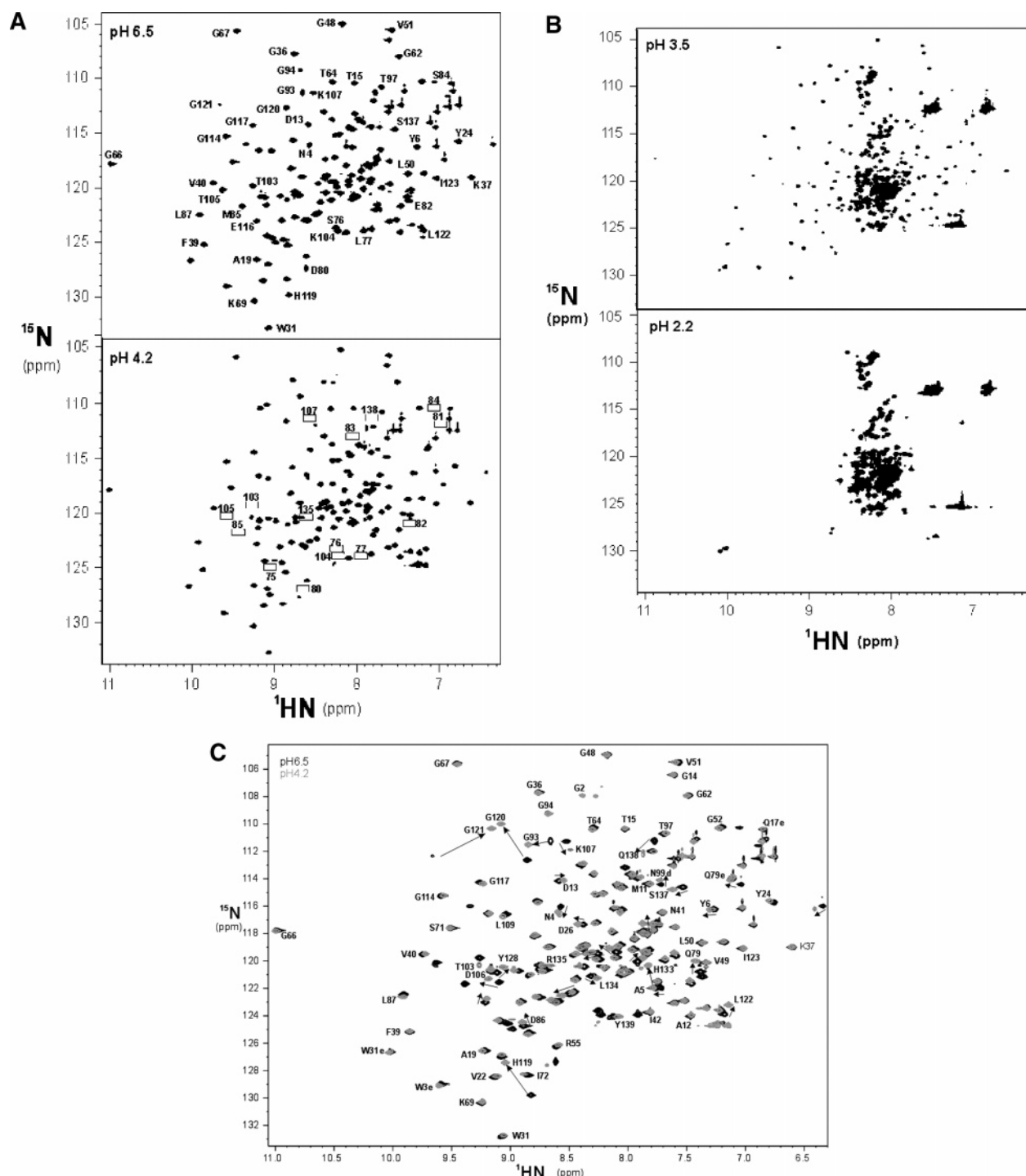
FIGURE 6: Acid titration of ^{15}N-labeled HPP monitored by 2D ^{1}H-^{15}N HSQC NMR spectroscopy. The 2D ^{1}H-^{15}N HSQC spectra of HPP at pH 6.5, 4.2 (panel A), 3.5, and 2.2 (panel B) are shown at equilibrium. Each sample contains approximately 1 mM HPP buffered in 10 mM citrate-phosphate and 1 mM DTT at 20 °C. The panel containing the spectrum at pH 6.5 serves as the reference for serial titration points, and the ^{1}H-^{15}N cross-peaks were labeled according to the published assignments of Metzler et al. (39). A subset of the residues that broaden (disappear) during the course of the titration is boxed in the pH 4.2 spectrum and is labeled at the native chemical shift. Superposition of the 2D ^{1}H-^{15}N HSQC spectra of native HPP (pH 6.5) and the unfolding intermediate (pH 4.2) is shown in panel C. The native HSQC spectrum is shown in black with the overlaid intermediate spectrum in gray. The arrows indicate the direction of the chemical shift change, and nonoverlapping cross-peaks are assigned at the intermediate species chemical shift.

similar to that of the pH 7.0 species under identical conditions and is further evidence that the overall topology of the pH 4.0 species is nativelike and is not aggregated. In contrast, a measured D_s value of 0.73×10^{-6} cm^2/s for the pH 2.0 species is consistent with a loss of compactness.

Acid-Induced Unfolding of HPP Monitored by 2D ^{1}H-^{15}N HSQC. The acid-induced unfolding of HPP from pH 6.5 to

2.0 was monitored by 2D ^{1}H-^{15}N HSQC NMR spectroscopy to specifically identify the pH-responsive residues (Figure 6). As seen in Figure 6A, the native spectrum at pH 6.5 is well dispersed with sharp nonoverlapping lines, characteristic features of a properly folded polypeptide chain. This allowed the assignment of all backbone amide (nonproline) cross-peaks in the native ^{1}H-^{15}N HSQC spectrum as published by

Table 2: Apparent pK_a Values of Titrating Residues[a]

residue number	apparent pK_a
R74	4.33
Q79	4.4
D86	4.98
R88	5.49
V100	4.35
T101	5.01
T103	5.91
K104	5.4
D106	4.9
K107	4.8
L110	5.49
V118	5.51
H119	5.45
G120	5.3
G121	5.26
L122	5.65
N124	5.75
K125	4.61
Y128	4.81
E129	4.02
A131	6.41
H133	5.72
L134	5.22
R135	5.88
R136	5.75

[a] The pK_a values were obtained for the curves shown in Figure 8 from pH 7.5 to 3.8.

Metzler et al (*37*). The assignment of the perturbed cross-peaks in subsequent spectra was accomplished by comparing successive spectra, beginning with the native spectrum and tracking the titrating resonances; however, the spectral overlap below pH 4.0 precluded further assignments. The chemical shifts of 49 of the 133 observable residues exhibited pH dependence throughout the titration series. The perturbed cross-peaks corresponded to residues with both ionizeable and nonionizeable side chains and are listed in Table 2. The dramatic effect of decreasing pH on backbone resonances can be seen in panel 6A (pH 4.2). The boxes positioned at the native backbone chemical shift for Asp 75, Ser 76, Leu 77, Leu 78, Asp 80, Gly 81, Glu 82, Phe 83, Ser 84, Met 85, Thr 103, Lys 104, Thr 105, and Lys 107 represent broadened cross-peaks. Line-broadening is consistent with slow conformational exchange in the ms to μs regime and indicates increased backbone flexibility, which is compatible with local unfolding of the polypeptide chain (*38*). In addition, the signal intensities of a number of cross-peaks gradually diminish, concomitant with the appearance of non-native cross-peaks. For example, two cross-peaks assigned to Gly 2 at pH 4.2 are well populated in the titration series beginning at pH 6.0 and persist to pH 2.0. This is evidence that the *N*-terminus is dynamic, undergoing a slow exchange between unfolded conformations (panel 6A). As seen in panel 6B, the highly structured intermediate species and the unfolded species are in conformational exchange, and further acidification drives the equilibrium toward the unfolded state. The loss of spectral dispersion at pH 2.0 is consistent with the unfolding of the polypeptide chain. Specifically, the H_N chemical shift distribution collapses to 7.9−8.55 ppm in the ^{1}H dimension, which is characteristic of an unfolded polypeptide chain (as confirmed by CD and tryptophan fluorescence data) (*39, 40*). A superposition of the native state ^{1}H-^{15}N HSQC spectrum and the equilibrium intermedi-
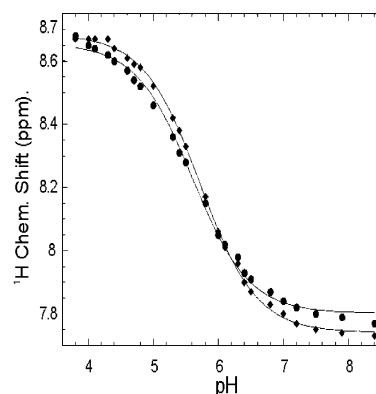

FIGURE 7: Titration of His 119 and His 133 by 1D ^{1}H NMR spectroscopy. The plots of the side-chain C2-^{1}H chemical shift vs pH (pH 8.5 to 4.0), for His 133 and His 119 in 100% D_2O are shown. The curves result from best fits of the Henderson−Hasselbach equation, and a pK_a value of 5.71 ± 0.01 was determined for His 133 (●) and 5.60 ± 0.02 for His 119 (◆).

ate state ^{1}H-^{15}N HSQC spectrum is shown in Figure 6C. Of the expected 135 backbone cross-peaks, 121 are visible in the pH 4.0 spectrum, and 39 exhibit varying degrees of perturbation. Residues experiencing non-native environments in the pH 4.2 species display altered line-width and/or significant chemical shift perturbation relative to those of the native state. In contrast, the 82 residues that remain in a nativelike environment at pH 4.2 exhibit narrow line-widths and identically superimpose with the spectrum at pH 6.5. Because a majority of the cross-peaks in the pH 4.0 spectrum are unperturbed, the topology and secondary structural content of the equilibrium unfolding intermediate is largely nativelike.

Titration of His 119 and His 133 monitored by 1D ^{1}H NMR. The pK_a values of His 119 and 133 were determined by pH titration of the imidazole group C2-^{1}H, monitored from pH 8.0 to 4.0 by 1D ^{1}H NMR spectroscopy in 100% D_2O. Below pH 4.0, the spectral lines broaden and begin to overlap, indicative of global conformational changes in HPP. The 1D ^{1}H NMR spectra in the basic regime are dominated by two narrow lines, which were assigned to the slowly exchanging C2-^{1}H of the only two histidines on HPP (assignments were obtained from unpublished ^{13}C-edited NMR experiments). Figure 7 shows a plot of the chemical shift as a function of pH, and the pK_a values for His 119 and His 133 in D_2O were determined to be 5.60 ± 0.02 and 5.71 ± 0.01, respectively from a nonlinear fit of the data. These pK_a values are expected to be slightly higher in H_2O by 0.06 (*41*). Importantly, the calculated pK_a values coincide with the midpoint of the transition between the native and the acid-induced equilibrium intermediate. Moreover, the pH-dependence of a number of cross-peaks (N → I) tracks with the titration behavior of either His 119 or His 133 (Figure 8 and Table 2). These results suggest that the ionization state of one or both His residues influence the overall stability of native HPP and modulate the formation of the intermediate species.

DISCUSSION

Structural Description of the Low pH Equilibrium Intermediate. Assignment of the 2D ^{1}H-^{15}N HSQC spectrum at pH 4 unambiguously identified regions on HPP that exhibit
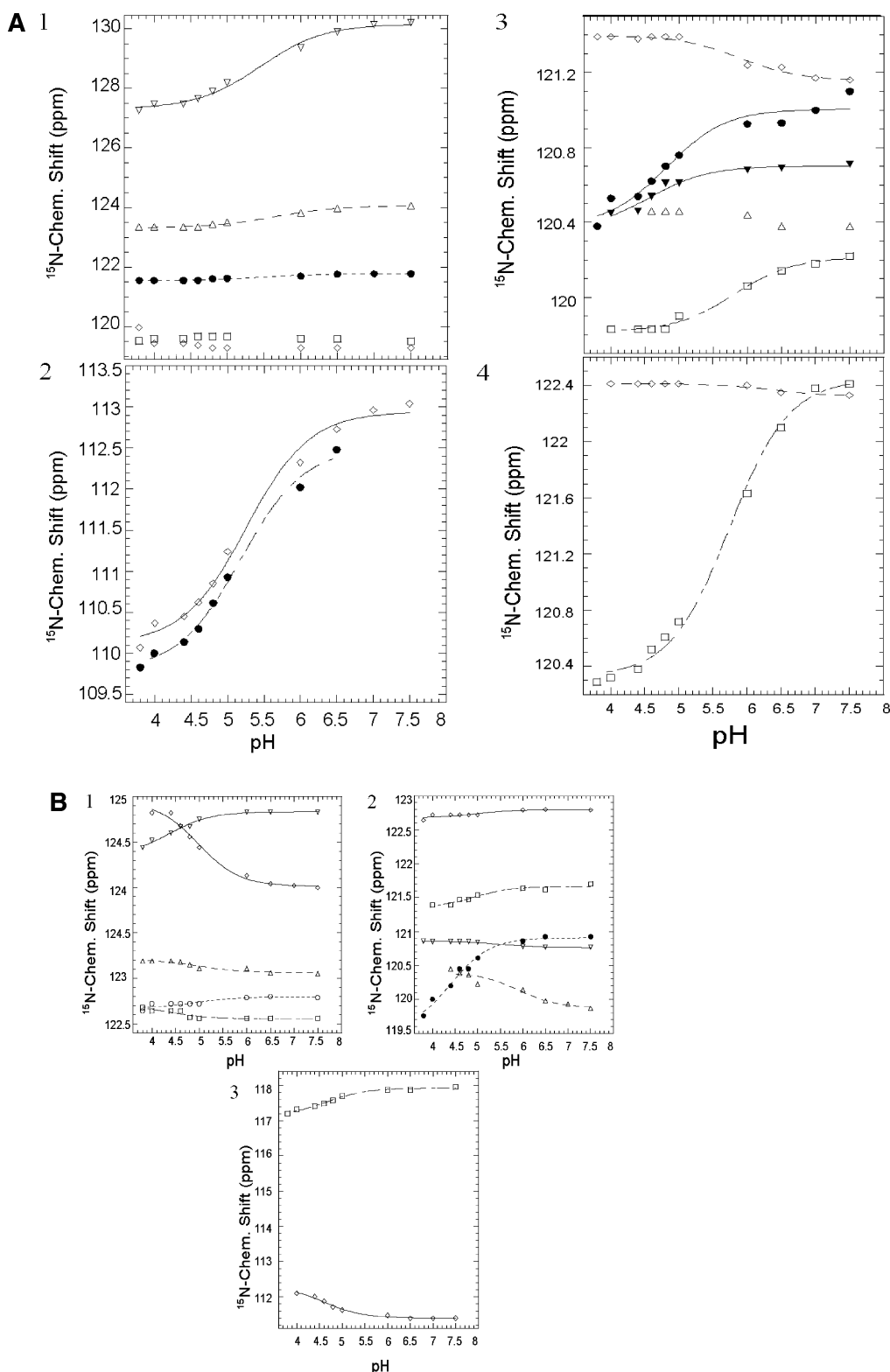
FIGURE 8: Plots of the amide nitrogen chemical shift vs pH for select residues. The chemical shift change as a function of pH (pH 7.5−3.8) for perturbed residues were extracted from a series of ¹H-¹⁵N HSQC spectra acquired in a manner identical to that used for the set shown in Figure 6. The solid lines represent best fits to the Henderson−Hasselbach equation as described in Materials and Methods. (A) α-helix 4 ¹⁵N chemical shift vs pH; panel 1 (*N*-terminus): V118 (●), H119 (▽), L122 (△), I124 (□), K125 (◇). Panel 2: G120 (◇), G121 (●). Panels 3 and 4: *C*-terminal residues of α-helix 4 ¹⁵N chemical shift vs pH; Panel 3: Y128 (●), E129 (▼), L134 (◇), R135 (△), R136 (□). Panel 4: A131 (◇), H133 (□). (B) ¹⁵N-chemical shift vs pH for a subset of the residues that include the *β*-sheet region. Panel 1: D86 (▽), K104 (◇), T101 (△), L110 (○), V100 (□); panel 2: Q79 (◇), D106 (□), R88 (▽), T103 (△), L110 (●); panel 3: R74 (□), K107 (◇).

non-native structure. Figure 9 shows the 3D structure of native HPP color coded according to the change in chemical shift as a function of pH (*42*). The perturbed residues map to α-helices 1 and 4, *β*-strands 4, 5, and 6 and connecting

loops, and residues located in the hydrophobic core. The residues that comprise the hydrophobic core on HPP were determined previously from the refined solution NMR structure (*43*). For example, the rigid hydrophobic core of
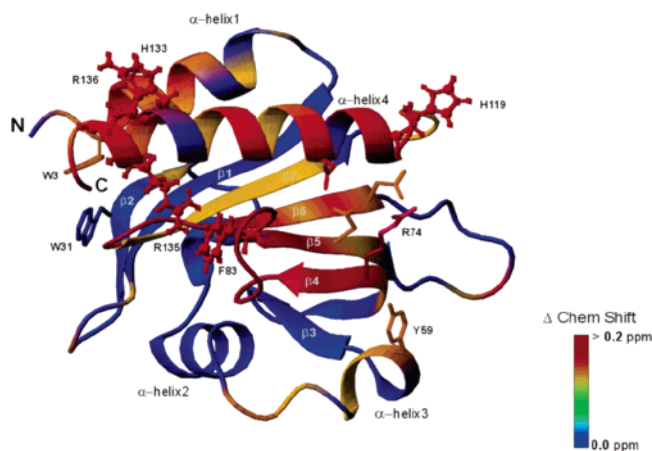
FIGURE 9: Residues that change significantly at pH 4.0 are mapped onto the 3D X-ray crystal structure of profilin. The change in chemical shift in the ^{1}H-dimension and ^{15}N-dimension are quantitated using the equation below according to Farmer et al. (*42*), $[({}^{1}H)^{2} + (0.0289)({}^{15}N)^{2}]^{1/2}$. Residues exhibiting no change in chemical shift are colored blue; 0.06−0.1 ppm are colored yellow; 0.1−0.2 ppm are colored orange; and >0.2 ppm are colored red. The residues exhibiting the largest Δ-chemical shift are located on α-helices 1 and 4 and β-strands 4, 5, and 6. These residues span the actin and poly-L-proline binding surfaces.

native HPP, which consists of residues Ala 20, Val 22, Phe 39, Ile 42, Val 47, Leu 50, Val 51, Leu 63, Leu 65, Cys 70, Val 72, Leu 77, Leu 78, Met 85, Leu 87, Val 100, Val 102, Leu 109, Leu 111, and Met 113, is relatively inaccessible to the solvent as probed by ANS binding (Figure 3). A subset of these residues, including Val 72, Leu 77, Leu 78, Met 85, Val 100, and Val 102, exhibit varying degrees of chemical shift alteration and severe line-broadening, indicating that the hydrophobic core in the intermediate species is structurally distinct relative to that of the native species. However, the hydrophobic core remains largely solvent inaccessible (Figure 3) in the folding intermediate. Nevertheless, the broadened cross-peaks, comprising residues Arg 74−Met 85 and Met 103−Thr 108 (Figure 6A) are clear evidence that the rigid β-sheet core exhibited by HPP in the native conformation is altered at pH 4.

The hydrophobic core of HPP is shielded from solvent as a result of tertiary interactions between the β-sheet core and the surrounding four α-helices (Figure 1). Interestingly, two new cross-peaks, which are assigned to Gly 2, are prominent in the pH 4 spectrum, and similarly, Asn 4 and Tyr 6 (solvent exposed) also exhibit two cross-peaks, which is an indication that the N-terminus of α-helix1 is undergoing slow conformational exchange (Figure 6). α-Helix4 is adjacent to α-helix1, and a majority of the residues are perturbed at low pH (His 119−Lys 125, Tyr 128−Met 130, and His 133−Tyr 139), signifying structural rearrangements in the poly-L-proline binding site. It is noteworthy, that residues that are adjacent to His 119 and His 133 reflect a titration profile similar to that of the histidines. Importantly, the amino acid residues on α-helix 4 interact directly with the β-sheet of HPP via side chain−side chain contacts, consequently bridging distal sites that exhibit significant structural perturbations, that is, Arg 135 on α-helix 4 and Phe 83 on β-strand 5. It appears that local, discrete changes in the tight tertiary packing could account for the increase in the solvent-exposed surface of the intermediate species supported by the change in ANS fluorescence. Additionally, the broadened

cross-peaks observed in the 2D HSQC spectra likely correspond to an increased plasticity in the polypeptide chain.

Correlation between His pK$_a$ and Intermediate Formation. A number of cross-peaks that were assigned to nonpolar residues exhibited a chemical shift dependence on pH, that is, Ala 5, Val 72, Ile 73, Leu 77, Leu 78, Gly 81, Phe 83, Met 85, Gly 93, Val 100, Thr 101, Thr 103, Thr 105, Thr 108, Gly 120, Gly 121, Leu 122, Ile 128, Met 130, and Leu 134. Figure 8 depict plots of the pH-dependent chemical shift change of both polar and nonpolar residues from pH 7.5−3.5. Because the chemical shift of each residue is sensitive to the local environment, a change in chemical shift signals an altered environment and backbone conformation (*44*). Moreover, the pH sensitivity of the nonpolar residues is likely a consequence of the influence of vicinal charged groups (i.e., His) on the proximal nonpolar residues. For example, Gly 120 and Gly 121 ^{15}N titration profile reflects the trace and pK$_a$ of His 119. Similarly, the titration curves of Leu 134 and Arg 136 ^{15}N chemical shift profiles correspond to His 133. Clearly, the ionization state of His 119 and His 133 on α-helix 4 has dramatic effects on the stability of the native fold and contributes to the formation of the intermediate species. Whereas His 119, which is located N-terminal to α-helix 4 is exposed to the solvent, His 133 is located near the C-terminus of α-helix 4 and is partially buried in a hydrophobic groove that serves as the polyproline ligand binding site. The measured side chain pK$_a$ values of His119 and His133 are 5.6 and 5.7, respectively, and are approximately 0.5 pH units lower than the usual pK$_a$ values of the histidine side chain (*45*, *46*). More importantly, these pK$_a$ values coincide with the midpoint of the transition between native and intermediate states and suggest that the protonation of one or both histidine residues is responsible for the transition. Protein folding studies using apomyoglobin and cytochrome *c* as models have demonstrated the effect of charged His residues on protein stability. In the case of apomyoglobin, a non-native conformation has been attributed to the protonation of buried histidine residues with acidic pK$_a$ values (*47*). The cytochrome *c* molten globule unfolding intermediate can be promoted by the disruption of a salt-bridge between His 26 and Glu 44, which stabilizes an important omega-loop (*48*).

Residues that Undergo the Largest Chemical Shift Changes at pH 4.0 Cluster at the Profilin−G-Actin Interface. As shown in Figure 9, the bulk of the residues experiencing the greatest pH-associated perturbations map to the amino terminus of α-helix1, α-helix3, throughout α-helix4, and portions of β-strands 4, 5, and 6. In particular, His119−Asn124 and Glu129 on α-helix4, which contact subdomain1 on G-actin, are altered in the intermediate conformation. Additionally, the residues that make specific contacts with subdomain3 on G-actin, that is, Ile 73, Arg 74, Glu 82, Ser 84 and Asp 86 on β-strands 4 and 5, exhibit distinctly different chemical shifts. Approximately 12 out of the 19 residues that make specific contact with G-actin exhibit non-native chemical shifts in the intermediate conformation, suggesting an altered G-actin binding surface. The pH-sensitive residues on HPP that make specific contributions to the G-actin binding surface are highlighted in Table 3. A number of residues, including Asp 75−Met 85 and Thr 103−Thr 105 that span β-strands 4, 5, and 6, and are integral to the hydrophobic core of HPP, exhibit severe line broadening

Table 3: Residues at the Poly-L-pro−Profilin−Actin Interface and Shifted Residues at pH 4

profilin−actin	actin−profilin	profilin−poly-L-pro site	perturbed residues at pH 4.0
Y59	H173	W3 Y6 W31 H133 Y139	W3 N4 A5 Y6 D8 N9 D13
V60	R290 V267		Y24 D26 R55 Y59
S71	D286 Y290		V72 I73 R74−S84 M85 D86
I73	P172 Y169		N99 V100 T101V102 T103
R74	H371		K104 T105 D106 K107 T108
E82	K113		H119 G120 G121 L122 N124
S84	R372		K125 Y128 E129 M130 H133
D86	R372		L134 R135 R136 S137 Q138
R88	E167 Y169		Y139
T89	Y166		
K90	D286 D288		
T97	E167		
N99	Y169		
H119	Y169 Y133		
	K373		
G120	Y169		
G121	R372 K373		
N124	R372		
K125	E361 E364		
E129	E364		

in the low pH spectra. This line broadening results from the intermediate conformational exchange between distinct environments and suggests that this segment of the β-sheet structure is less rigid than the other segments of the polypeptide chain. Potentially, the structural changes observed for α-helix 4 and the β-sheet region of HPP could preclude G-actin binding.

Functional Significance of the Intermediate Conformation. The role of electrostatics on profilin−ligand interactions has been investigated in vitro and in vivo. The earliest studies reported that the profilin−G-actin complex could be disrupted below pH 6.0, suggesting a role for electrostatics in complex formation (*49*). Additionally, Lassing and Lindberg reported that the highly charged phospholipid PIP$_2$ can dissociate the profilin−G-actin complex (*50*). Recently, mutational analysis confirmed that His 119 on profilin is essential for G-actin binding because the substitution of His 119 with Glu abolishes G-actin binding (*51*). The mutation of His 133 to Ser 133 abrogates profilin−poly-L-proline binding in vitro, and this mutation has been demonstrated to exhibit potent tumor suppression activities in vivo, which highlights the functional significance of complimentary charge preservation on ligand binding (*52, 53*). Another important determinant for ligand binding is the structure and orientation of the critical residues constituting the actin binding interface. Specifically, the X-ray crystal structure of the profilin−β-actin complex revealed an extensive binding interface, covering a total surface area of 2250 Å^2 (*49*). This underscores the significance of preserving the structure and geometry of residues on profilin that specifically contact G-actin at the interface. Additionally, the conformations of profilin free in solution and bound to ligand (G-actin or poly-L-proline) almost superimpose, which highlights the importance of binding surface topology for ligand recognition and complex formation. The chemical shifts of 12 of the 19 residues on profilin that contact G-actin (Table 3) are significantly altered in the non-native state. For example, residue Ile 73 on profilin 1 makes specific contact with Pro 172 and Tyr 290 on β-actin, Arg 74 interacts with His 371, Glu 82 contacts Lys 113, Ser 84 contacts Arg 372, Asp 86 contacts Arg 372, Asn 99 contacts Tyr 169, His 119 contacts Tyr 169, Tyr 133 and Lys 373, Gly 120

contacts Tyr 169, Gly 121 contacts Arg 372 and Lys 373, Asn 124 contacts Arg 372, Lys 125 contacts Glu 361 and Glu 364, and Glu 129 contacts Glu 364. The significance of preserving specific interactions at the profilin−G-actin interface in the formation of a stable profilin−G-actin complex was demonstrated by the substitution of Val 60 to Glu and Gly 120 to Phe (residues on profilin 1 involved in forming a stable profilin−G-actin complex), which impaired the interaction (*54*). It has been reported that the deletion of the last eight C-terminal residues of *Acanthamoeba* profilin 2 resulted in a conformation that exhibited features consistent with a molten globule (near-native secondary structure and greatly reduced tertiary interactions) and reduced G-actin binding potential (*55*). In a similar manner, the pH-dependent conformational change, which is observed throughout the last 20 C-terminal residues and β-sheet region on HPP, may be sufficient for G-actin release.

The non-native conformation of HPP may be significant for G-actin release at the cell membrane. The environment immediately proximal to the highly anionic inner-leaflet of the plasma membrane is reportedly 1 to 2 pH units less than bulk pH (*23, 24*), and recent evidence suggests that raft-like domains enriched in phosphoinositides form discrete clusters in the membrane (*25, 26, 56−58*). The physical properties of these microdomains are expected to be distinct with respect to many physiological characteristics, such as pH, dielectric constants, ionic concentration, and ligand concentration, which will determine the average protein conformational states. Indeed, studies have shown that histidine pK_a values vary with the local environment, such as salt concentration, binding interaction, and side-chain burial, thereby allowing the environment to select/switch between allowable backbone conformations (*59, 60*). Furthermore, the CD profile and ANS binding show that the transition to the intermediate conformation begins at approximately pH 6.4, suggesting that a local decrease of $\sim$0.6 pH units would be sufficient to promote the near-native intermediate conformation at the cell membrane. Reportedly, non-native states have been demonstrated to facilitate peripheral membrane protein binding and insertion, as in the case of colicin A pore-forming domain and α-lactalbumin (*22, 61, 62*).

In summary, these studies examined a pH-induced equilibrium intermediate of HPP and revealed a subset of the accessible conformational states encoded in the primary sequence of HPP, which may be consistent with the physicochemical properties that exist in proximity to the plasma membrane. Our observations suggest that a novel mechanism for dissociation of the HPP−G-actin and HPP−poly-L-proline complexes at the cell membrane involves unfolding or partial unfolding of profilin. Potentially, a non-native conformation such as the species elucidated in these studies may become fully populated upon localization to the leading edge, thus abolishing G-actin sequestration and increasing the local concentration of available G-actin for rapid filament assembly and cell propulsion.

REFERENCES

1. Kwiatkowski, D. J., and Bruns, G. A. (1988) Human profilin. Molecular cloning, sequence comparison, and chromosomal analysis, *J. Biol. Chem. 263*, 5910−5915.
2. Magdolen, V., Oechsner, U., Muller, G., and Bandlow, W. (1988) The intron-containing gene for yeast profilin (PFY) encodes a vital function, *Mol. Cell. Biol. 8*, 5108−5115.
3. Verheyen, E. M., and Cooley, L. (1994) Profilin mutations disrupt multiple actin-dependent processes during Drosophila development, *Development 120*, 717−728.
4. Honore, B., Madsen, P., Andersen, A. H., and Leffers, H. (1993) Cloning and expression of a novel human profilin variant, profilin II, *FEBS Lett. 330*, 151−155.
5. Lambrechts, A., Verschelde, J. L., Jonckheere, V., Goethals, M., Vandekerckhove, J., and Ampe, C. (1997) The mammalian profilin isoforms display complementary affinities for PIP2 and proline-rich sequences, *EMBO J. 16*, 484−494.
6. Carlsson, L., Nystrom, L. E., Sundkvist, I., Markey, F., and Lindberg, U. (1977) Actin polymerizability is influenced by profilin, a low molecular weight protein in nonmuscle cells, *J. Mol. Biol. 115*, 465−483.
7. Pollard, T. D., and Cooper, J. A. (1984) Quantitative analysis of the effect of Acanthamoeba profilin on actin filament nucleation and elongation, *Biochemistry 23*, 6631−66341.
8. Goldschmidt-Clermont, P. J., Furman, M. I., Wachsstock, D., Safer, D., Nachmias, V. T., and Pollard, T. D. (1992) The control of actin nucleotide exchange by thymosin beta 4 and profilin. A potential regulatory mechanism for actin polymerization in cells, *Mol. Biol. Cell 3*, 1015−1024.
9. Pantaloni, D., and Carlier, M. F. (1993) How profilin promotes actin filament assembly in the presence of thymosin beta 4, *Cell 75*, 1007−1014.
10. Theriot, J. A., and Mitchison, T. J. (1993) The three faces of profilin, *Cell 75*, 835−838.
11. Goldschmidt-Clermont, P. J., Machesky, L. M., Baldassare, J. J., and Pollard, T. D. (1990) The actin-binding protein profilin binds to PIP2 and inhibits its hydrolysis by phospholipase C, *Science 247*, 1575−1578.
12. Goldschmidt-Clermont, P. J., Kim, J. W., Machesky, L. M., Rhee, S. G., and Pollard, T. D. (1991) Regulation of phospholipase C-gamma 1 by profilin and tyrosine phosphorylation, *Science 251*, 1231−1233.
13. Mahoney, N. M., Rozwarski, D. A., Fedorov, E., Fedorov, A. A., and Almo, S. C. (1999) Profilin binds proline-rich ligands in two distinct amide backbone orientations, *Nat. Struct. Biol. 6*, 666−671.
14. Mahoney, N. M., Janmey, P. A., and Almo, S. C. (1997) Structure of the profilin-poly-L-proline complex involved in morphogenesis and cytoskeletal regulation, *Nat. Struct. Biol. 4*, 953−960.
15. Ramesh, N., Anton, I. M., Hartwig, J. H., and Geha, R. S. (1997) WIP, a protein associated with wiskott-aldrich syndrome protein, induces actin polymerization and redistribution in lymphoid cells, *Proc. Natl. Acad. Sci. U.S.A. 94*, 14671−14676.
16. Zhao, W. M., Jiang, C., Kroll, T. T., and Huber, P. W. (2001) A proline-rich protein binds to the localization element of Xenopus Vg1 mRNA and to ligands involved in actin polymerization, *EMBO J. 20*, 2315−2325.
17. Ozaki-Kuroda, K., Yamamoto, Y., Nohara, H., Kinoshita, M., Fujiwara, T., Irie, K., and Takai, Y. (2001) Dynamic localization and function of Bni1p at the sites of directed growth in *Saccharomyces cerevisiae*, *Mol. Cell. Biol. 21*, 827−839.
18. Evangelista, M., Blundell, K., Longtine, M. S., Chow, C. J., Adames, N., Pringle, J. R., Peter, M., and Boone, C. (1997) Bni1p, a yeast formin linking cdc42p and the actin cytoskeleton during polarized morphogenesis, *Science 276*, 118−22.
19. Ostrander, D. B., Gorman, J. A., and Carman, G. M. (1995) Regulation of profilin localization in *Saccharomyces cerevisiae* by phosphoinositide metabolism, *J. Biol. Chem. 270*, 27045−27050.
20. Hartwig, J. H., Chambers, K. A., Hopcia, K. L., and Kwiatkowski, D. J. (1989) Association of profilin with filament-free regions of human leukocyte and platelet membranes and reversible membrane binding during platelet activation, *J. Cell Biol. 109*, 1571−1579.
21. Bubb, M. R., Baines, I. C., and Korn, E. D. (1998) Localization of actobindin, profilin I, profilin II, and phosphatidylinositol-4,5-bisphosphate (PIP2) in Acanthamoeba castellanii, *Cell Motil. Cytoskeleton 39*, 134−146.
22. van der Goot, F. G., Gonzalez-Manas, J. M., Lakey, J. H., and Pattus, F. (1991) A 'molten-globule' membrane-insertion intermediate of the pore-forming domain of colicin A, *Nature 354*, 408−410.
23. Prats, M., Teissie, J., and Tocanne, J. F. (1986) Lateral proton conduction at lipid-water interfaces and its implications for the chemiosmotic-coupling hypothesis, *Nature 322*, 756−758.
24. Bychkova, V. E., Dujsekina, A. E., Klenin, S. I., Tiktopulo, E. I., Uversky, V. N., and Ptitsyn, O. B. (1996) Molten globule-like state of cytochrome *c* under conditions simulating those near the membrane surface, *Biochemistry 35*, 6058−6063.
25. Tall, E. G., Spector, I., Pentyala, S. N., Bitter, I., and Rebecchi, M. J. (2000) Dynamics of phosphatidylinositol 4,5-bisphosphate in actin-rich structures, *Curr. Biol. 10*, 743−746.
26. Honda, A., Nogami, M., Yokozeki, T., Yamazaki, M., Nakamura, H., Watanabe, H., Kawamoto, K., Nakayama, K., Morris, A. J., Frohman, M. A., and Kanaho, Y. (1999) Phosphatidylinositol 4-phosphate 5-kinase alpha is a downstream effector of the small G protein ARF6 in membrane ruffle formation, *Cell 99*, 521−32.
27. Ptitsyn, O. B. (1995) Molten globule and protein folding, *Adv. Protein. Chem. 47*, 83−229.
28. Sandvig, K., et al. (1986) Requirement of a transmembrane pH gradient for the entry of diphtheria toxin into cells at low pH, *J. Biol. Chem. 261*, 11639−11644.
29. Huang, S., Ratliff, K. S., and Matouschek, A. (2002) Protein unfolding by the mitochondrial membrane potential, *Nat. Struct. Biol. 9*, 301−307.
30. Lindberg, U., Schutt, C. E., Hellsten, E., Tjader, A. C., and Hult, T. (1988) The use of poly(L-proline)-sepharose in the isolation of profilin and profilactin complexes, *Biochim. Biophys. Acta 967*, 391−400.
31. Zhang, O., Kay, L. E., Olivier, J. P., and Forman-Kay, J. D. (1994) Backbone 1H and 15N resonance assignments of the N-terminal SH3 domain of drk in folded and unfolded states using enhanced-sensitivity pulsed field gradient NMR techniques, *J. Biomol. NMR 4*, 845−858.
32. Altieri, A. S., Hinton, D. P., and Byrd, R. A. (1995) Association of biomolecular systems via pulsed field gradient NMR self-diffusion measurements, *J. Am. Chem. Soc. 117*, 7566−7567.
33. Dubin, S. B., Clark, N. A. and Benedek, G. B. (1971) *J. Chem. Phys. 54*, 5158−5164.
34. Piotto, M., Saudek, V., and Sklenar, V. (1992) Gradient-tailored excitation for single-quantum NMR spectroscopy of aqueous solutions, *J. Biomol. NMR 2*, 661−665.
35. Santoro, M. M., and Bolen, D. W. (1988) Unfolding free energy changes determined by the linear extrapolation method. 1. Unfolding of phenylmethanesulfonyl alpha-chymotrypsin using different denaturants, *Biochemistry 27*, 8063−8068.
36. Semisotnov, G. V., Rodionova, N. A., Razgulyaev, O. I., Uversky, V. N., Gripas', A. F., and Gilmanshin, R. I. (1991) Study of the "molten globule" intermediate state in protein folding by a hydrophobic fluorescent probe, *Biopolymers 31*, 119−28.
37. Metzler, W. J., Constantine, K. L., Friedrichs, M. S., Bell, A. J., Ernst, E. G., Lavoie, T. B., and Mueller, L. (1993) Characterization of the three-dimensional solution structure of human profilin: 1H, 13C, and 15N NMR assignments and global folding pattern, *Biochemistry 32*, 13818−29.
38. Palmer III, A. G., Williams, J., and McDermott, A. (1996) Nuclear magnetic resonance studies of biopolymer dynamics, *J. Phys. Chem. 100*, 13293−13310.

39. Wishart, D. S., Sykes, B. D., and Richards, F. M. (1991) Relationship between nuclear magnetic resonance chemical shift and protein secondary structure, *J. Mol. Biol. 222*, 311−333.

40. Yao, J., Dyson, H. J., and Wright, P. E. (1997) Chemical shift dispersion and secondary structure prediction in unfolded and partly folded proteins, *FEBS Lett. 419*, 285−289.

41. Bundi, A., and Wuthrich, K. (1979) *Biopolymers 18*, 285.

42. Farmer, B. T., II, Constantine, K. L., Goldfarb, V., Friedrichs, M. S., Wittekind, M., Yanchunas, J., Jr., Robertson, J. G., and Mueller, L. (1996) Localizing the NADP+ binding site on the MurB enzyme by NMR, *Nat. Struct. Biol. 3*, 995−997.

43. Metzler, W. J., Farmer, B. T., II, Constantine, K. L., Friedrichs, M. S., Lavoie, T., and Mueller, L. (1995) Refined solution structure of human profilin I, *Protein Sci. 4*, 450−459.

44. Bundi, A., and Wuthrich, K. (1977) 1H NMR titration shifts of amide proton resonances in polypeptide chains, *FEBS Lett. 77*, 11−14.

45. Tanokura, M. (1983) 1H NMR study on the tautomerism of the imidazole ring of histidine residues. I. Microscopic p*K* values and molar ratios of tautomers in histidine-containing peptides, *Biochim. Biophys. Acta 742*, 576−585.

46. Nozaki, Y., and Tanford, C. (1967) Intrinsic dissociation constants of aspartyl and glutamyl carboxyl groups, *J. Biol. Chem. 242*, 4731−4735.

47. Geierstanger, B., Jamin, M., Volkman, B. F., and Baldwin, R. L. (1998) Protonation behavior of histidine 24 and histidine 119 in forming the pH 4 folding intermediate of apomyoglobin, *Biochemistry 37*, 4254−4265.

48. Sinibaldi, F., Piro, M. C., Howes, B. D., Smulevich, G., Ascoli, F., and Santucci, R. (2003) Rupture of the hydrogen bond linking two Omega-loops induces the molten globule state at neutral pH in cytochrome *c*, *Biochemistry 42*, 7604−7610.

49. Schutt, C. E., Myslik, J. C., Rozycki, M. D., Goonesekere, N. C., and Lindberg, U. (1993) The structure of crystalline profilin-beta-actin, *Nature 365*, 810−816.

50. Lassing, I., and Lindberg, U. (1985) Specific interaction between phosphatidylinositol 4,5-bisphosphate and profilactin, *Nature 314*, 472−474.

51. Suetsugu, S., Miki, H., and Takenawa, T. (1998) The essential role of profilin in the assembly of actin for microspike formation, *EMBO J. 17*, 6516−6526.

52. Bjorkegren-Sjogren, C., Korenbaum, E., Nordberg, P., Lindberg, U., and Karlsson, R. (1997) Isolation and characterization of two mutants of human profilin I that do not bind poly(L-proline), *FEBS Lett. 418*, 258−264.

53. Wittenmayer, N., Jandrig, B., Rothkegel, M., Schluter, K., Arnold, W., Haensch, W., Scherneck, S., and Jockusch, B. M. (2004) Tumor suppressor activity of profilin requires a functional actin binding site, *Mol. Biol. Cell 15*, 1600−1608.

54. Schluter, K., Jockusch, B. M., and Rothkegel, M. (1997) Profilins as regulators of actin dynamics, *Biochim. Biophys. Acta 1359*, 97−109.

55. Kaiser, D. A., and Pollard, T. D. (1996) Characterization of actin and poly-L-proline binding sites of Acanthamoeba profilin with monoclonal antibodies and by mutagenesis, *J. Mol. Biol. 256*, 89−107.

56. Laux, T., Fukami, K., Thelen, M., Golub, T., Frey, D., and Caroni, P. (2000) GAP43, MARCKS, and CAP23 modulate PI(4,5)P(2) at plasmalemmal rafts, and regulate cell cortex actin dynamics through a common mechanism, *J. Cell Biol. 149*, 1455−1472.

57. Rozelle, A. L., Machesky, L. M., Yamamoto, M., Driessens, M. H., Insall, R. H., Roth, M. G., Luby-Phelps, K., Marriott, G., Hall, A., and Yin, H. L. (2000) Phosphatidylinositol 4,5-bisphosphate induces actin-based movement of raft-enriched vesicles through WASP-Arp2/3. *Curr. Biol. 10*, 311−320.

58. Pike, L. J., and Casey, L. (1996) Localization and turnover of phosphatidylinositol 4,5-bisphosphate in caveolin-enriched membrane domains, *J. Biol. Chem. 271*, 26453−26456.

59. Huyghues-Despointes, B. M., Thurlkill, R. L., Daily, M. D., Schell, D., Briggs, J. M., Antosiewicz, J. M., Pace, C. N., and Scholtz, J. M. (2003) p*K* values of histidine residues in ribonuclease Sa: effect of salt and net charge, *J. Mol. Biol. 325*, 1093−1105.

60. Edgcomb, S. P., and Murphy, K. P. (2002) Variability in the pK_a of histidine side-chains correlates with burial within proteins, *Proteins 49*, 1−6.

61. Halskau, O., Froystein, N. A., Muga, A., and Martinez, A. (2002) The membrane-bound conformation of alpha-lactalbumin studied by NMR-monitored 1H exchange, *J. Mol. Biol. 321*, 99−110.

62. Agasoster, A. V., Halskau, O., Fuglebakk, E., Froystein, N. A., Muga, A., Holmsen, H., and Martinez, A. (2003) The interaction of peripheral proteins and membranes studied with alpha-lactalbumin and phospholipid bilayers of various compositions, *J. Biol. Chem. 278*, 21790−21797.

63. Mulder, F. A., Mittermaier, A., Hon, B., Dahlquist, F. W., and Kay, L. E. (2001) Studying excited states of proteins by NMR spectroscopy, *Nat. Struct. Biol. 8*, 932−935.

64. Witke, W., Podtelejnikov, A. V., Di Nardo, A., Sutherland, J. D., Gurniak, C. B., Dotti, C., and Mann, M. (1998) In mouse brain profilin I and profilin II associate with regulators of the endocytic pathway and actin assembly, *EMBO J. 17*, 967−976.

65. Hartl, F., U. and, and Martin, J. (1997) *Curr. Opin. Struct. Biol. 7*, 41−52.